A De Novo Virus-Like Topology for Synthetic Virions

James E. Noble,[†] Emiliana De Santis,[†] Jascindra Ravi,[†] Baptiste Lamarre,[†] Valeria Castelletto,[‡] Judith Mantell,[§] Santanu Ray,[∥] and Maxim G. Ryadnov*,[†]

[†]National Physical Laboratory, Hampton Road, Teddington TW11 0LW, United Kingdom
[‡]Department of Chemistry, University of Reading, Reading RG6 6AD, United Kingdom
[§]Wolfson Bio-imaging Facility, Department of Biochemistry, University of Bristol, Bristol BS8 1TD, United Kingdom
[∥]SET, University of Brighton, Brighton BN2 4GJ, United Kingdom

ⓢ *Supporting Information*

ABSTRACT: A de novo topology of virus-like assembly is reported. The design is a trifaceted coiled-coil peptide helix, which self-assembles into ultrasmall, monodisperse, anionic virus-like shells that encapsulate and transfer both RNA and DNA into human cells. Unlike existing artificial systems, these shells share the same physical characteristics of viruses being anionic, nonaggregating, abundant, hollow, and uniform in size, while effectively mediating gene silencing and transgene expression. These are the smallest virus-like structures reported to date, both synthetic and native, with the ability to adapt and transfer small and large nucleic acids. The design thus offers a promising solution for engineering bespoke artificial viruses with desired functions.

self-assembling subunit   virus-like topology   peptide shells as synthetic virions
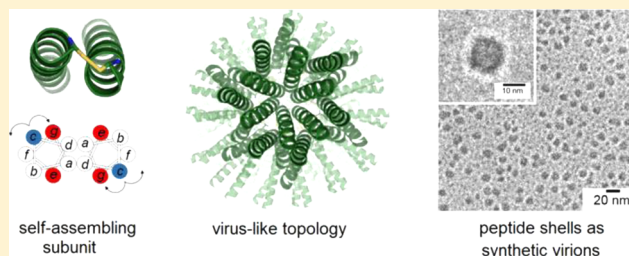
INTRODUCTION

Viruses are hollow nanoshells encasing nucleic acids.[1] The shells range from 17 nm (porcine circovirus)[2] to 1 μm (pandoravirus),[3] and all self-assemble from individual protein subunits.[1] The subunits are conserved protein folds programmed to reproduce the viral assembly, which inspires the search for synthetic analogues.[4] Different approaches and chemistries are being proposed, although a primary emphasis is often placed on applications rather than the structural cooperativity of viral designs.[5−10] As a result, amorphous, aggregating, and polydisperse structures are common products.[10] Recent peptide designs offer promising solutions.[11−13] However, these lack the morphological uniformity of viruses, while their ability to infect and mediate genetic processes remains to be demonstrated. Here, we introduce a de novo self-assembly topology, which mitigates these shortcomings and provides a biologically functional mimetic of the viral assembly.

The virus architecture adopts an *n*-fold rotational symmetry, where *n* can be 3 or 5 or both.[1] Therefore, adapting a virus-like structure requires a folding unit able to support at least a symmetric 3D (C_3) assembly.[14] A chemical approach to achieve this using relatively short peptide sequences, as opposed to fully folded proteins,[15] is to template the assembly of a folding unit on a macromolecular framework that can support the same properties of symmetry, monodispersity, and hierarchical assembly. In this regard, the dendrimer architecture lends itself as an intrinsic template for C_3-assembly.[16] Dendrimers are monodisperse, symmetric structures that are characterized by regular branching emanating from branching cells or hubs, which are covalent structures (Figure 1A).[17] Our design rationale is to convert such hubs into supramolecular focal points of folded peptides, thereby providing a self-assembling dendrimer-like topology (Figure 1B,C). Self-assembling or *tecto*-dendrimers were introduced as modular nanosphere clusters to benefit from the monodispersity and dimensional scaling of globular proteins.[18−20] These structures are analogous to viral particles in that both assemble from subunits around an inner focal point or cavity.[1,19,20] Thus, utilizing the dendrimer topology in a virus-like design serves the same benefits.

Advantages of this approach are reflected in recent peptide strategies that benefit from the symmetry-driven assembly of short peptide sequences locked into C_3-branching hubs.[11,13,14,21−23] The main focus in these strategies is to trigger the formation of extended networks closing into spherical particles.[23] To promote this mode of assembly, the arms of the units are made to adopt specific conformations (e.g., antiparallel β-sheets or parallel α-helical coiled coils), the type of which defines the spatial projections of the units with respect to one another in the assembly, that is, oblique[11,13] or orthogonal.[21,22] Because each C_3 unit must have three arms, one self-complementary sequence can be used in a covalent hub, enabling thus an oblique assembly via antiparallel interarm interactions,[13,14] whereas reported noncovalent hubs use naturally occurring sequences[11] or rely on the ability of several sequences to assemble into different building blocks that require covalent cross-linking to network.[21,22] Within these geometric constraints, specialist chemistry is necessary for covalent hubs, which limits their uptake and scale-up by
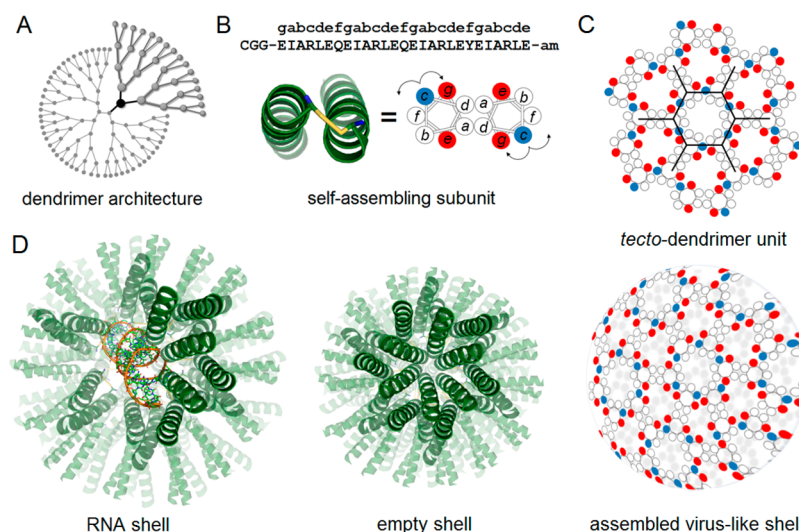
Figure 1. *tecto*-Dendrimeric virus-like (TecVir) design. (A) Schematic representation of the dendrimer architecture highlighting a branching cell (bold black) in a branch zoomed in for clarity. (B) TecVir sequence (top view) and its coiled-coil subunit (lower, left) configured into helical wheels with 3.5 residues per turn (lower, right). The subunit (PDB entry 4DMD rendered by PyMOL) highlights a cysteine bridge (yellow). The sequences show heptad repeats of canonical coiled coils, designated *gabcdef*. Residues at *a*, *d* sites form the hydrophobic interface, and are isoleucine and leucine, respectively, favoring dimer formation. Residues at *e* and *g* are anionic glutamates (red) that interact with cationic arginines (blue) at *c* forming intra-helical (*g*−*c*) interactions in the same dimer and inter-helical (*c*−*e′*) interactions between dimers. The arrows indicate intra- and interhelical interactions. (C) Each helix is a branching cell interacting with three other helices giving rise to a branching network (upper), which closes into a shell (lower). (D) 3D ribbon models of TecVir shells assembled without (right) and with siRNA (left). PDB entries 4DMD and 2F8S were adapted and rendered by PyMoL for coiled coils and siRNA, respectively. For clarity, all positively charged N-termini are shown as positioned inward toward the core of the shell (left) and toward siRNA in the core (right).

recombinant DNA technologies, while assemblies of several sequence types are stoichiometry-dependent,[22] which may lead to aberrant structures or superaggregation.[6,12,22] In this vein, an artificial single-sequence topology capable of C_3 assembly can provide an efficient design platform for emulating viruses, structurally and functionally. To advance the synthetic biology of artificial viruses, it is important that such a design generates homogeneous, nonaggregating shells that can be loaded with and deliver a biologically functional genetic material, the capability that has yet to be reported.

Recent developments of cargo encapsulation strategies in virus-like capsules assembled from viral peptide fragments[24,25] and in reassembled native viruses[26,27] provide evidence for controllable macro- and biomolecular encapsulation, suggesting the feasibility of biofunctional viral mimetics. In this light, our approach sets out to advance architectural virus-like designs with a generic and purely artificial topology supporting biologically functional viral mimetics.

■ RESULTS AND DISCUSSION

Peptide Design. With this in mind, we constructed a *tecto*-dendrimeric virus-like shell (TecVir). The design is based on a self-complementary coiled-coil subunit having three interfacial facets. The subunit is an α-helix, which self-pairs via a hydro-phobic interface typical of a coiled-coil dimer (Figure 1B).[28] In canonical coiled coils, each helix has one polar face and one hydrophobic face, which interact with counterpart helices, one in dimers and two in higher oligomers.[29] By contrast, in this design, each individual helix has one hydrophobic interface and two polar facets that are arranged to favor interactions with three other, but identical, neighbors (Figure 1B,C).[21] Each helix therefore can be viewed as a branching cell in a continuous branching network whose propagation axis runs perpendicular to that of individual helices (Figure 1B−D). All helices pack

laterally, but asymmetrically, because the geometry of hydro-phobic interfaces is different from that of the polar interfaces.[21,29] In a forming network, this mode of packing is encouraged to translate into a *trans*-helix asymmetry prompting spontaneous curvature in a manner similar to that of channel-forming proteins (e.g., TolC family)[30] or fluid lipid vesicles.[31] Polar facets in each TecVir helix support both inter- and intrahelical interactions (Figure 1B), making them concomitant along the aligned helices, which renders any changes in the entire electrostatic network highly cooperative or "fluid". Because the network at any stage of its assembly cannot be formed unless all three facets of each peptide are engaged, the edges of forming coiled-coil sheets cannot remain "sticky" and have to close on one another. Col-lectively, these factors facilitate the closure of an increasingly curved network into a shell.[14,21,22,31]

To support this transition, the peptide was extended at the N-terminus with a cysteine-containing motif CGG (Figure 1 and Table s1). The two-glycine linker separates cysteine residues from the coiled-coil framework in the sequence (Figure 1B) and allows only for N-terminal disulfide linkages that display N-terminal free amines on the forming coiled-coil sheets, but not within them. This feature excludes electrostatic repulsions between helices characteristic of other designs, which require compensating nonspecific orthogonal stabilization for coiled coils to propagate.[22] Instead, the trifaceted interhelix packing itself is expected to promote proximity-driven oxidation of cysteine residues, cementing the structure further. Thus, the cross-linking network of oxidized cysteines stabilizes interhelix interactions across the whole sheet surface without differ-entiating between the same or different coiled-coil dimers.[32] Such complementarity maintains the cooperative assembly of TecVir and thence the highly anisotropic packing of coiled coils into well hydrated and flexible sheets supporting, rather than restricting, their closure into spherical shells.[9,14,22] Without this
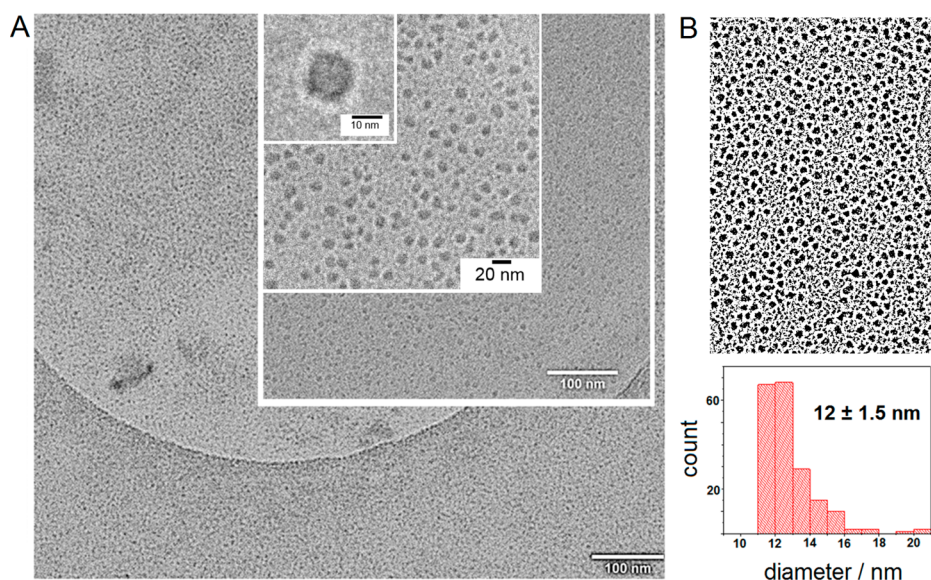
Figure 2. TecVir assembly. (A) Cryo-electron micrographs of assembled shells, and (B) a representative contrast-inverted image analysis.
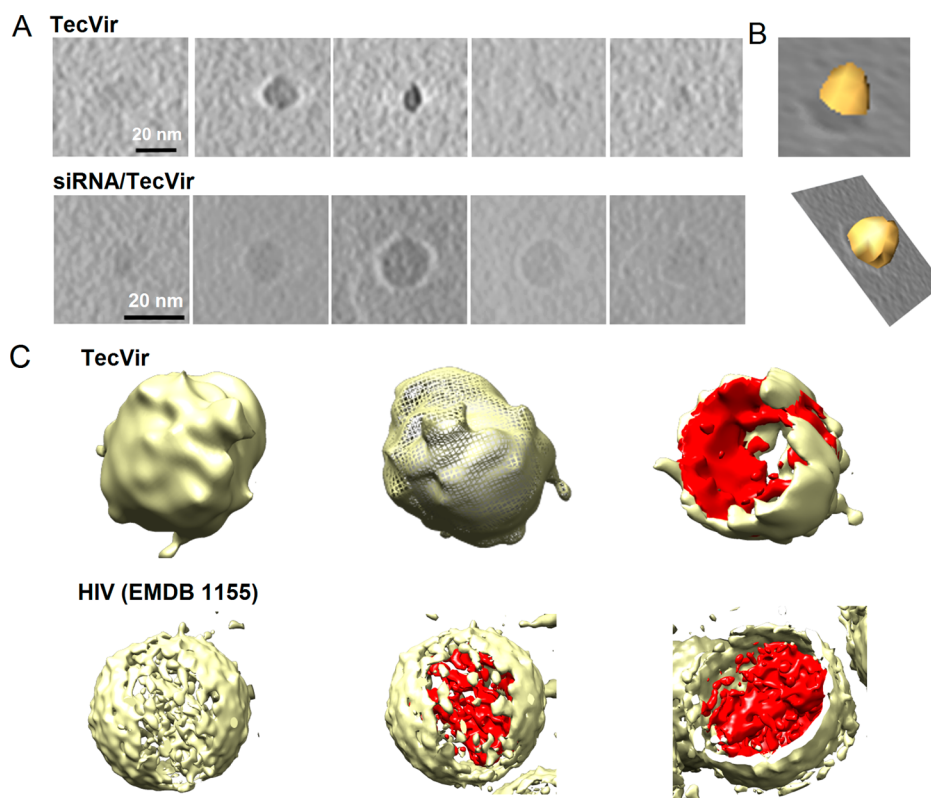
Figure 3. TecVir in 3D. (A) Cryo-electron tomography (z-planes) for TecVir alone and TecVir assembled with siRNA at the N/P molar ratio of 1/76 at 200 μM peptide, and (B) corresponding isosurface reconstructions. (C) 3D rendering of TecVir (upper) and HIV-1 core assembly (lower) (EMDataBank entry 1155)[37] shown for comparison. Note: Not to scale, HIV particles are >100 nm in diameter. TecVir: Volume reconstruction (left), the volume shown as a mesh and fitted to a sphere with a radius of 10 nm (center) and a reconstruction showing the exterior of the capsule in yellow and the interior in red (right). HIV-1: The volume reconstruction (left), the exterior and interior in yellow and red, respectively (center and right). Molecular graphics and analyses were performed with the UCSF Chimera package. Chimera is developed by the Resource for Biocomputing, Visualization, and Informatics at the University of California, San Francisco (supported by NIGMS P41-GM103311).[36]

cementing effect of oxidized cysteines, the C_3-symmetric networks would not be complete, resulting in more anisotropic assemblies such as nanofibers.[13]

Assembly and Folding. Consistent with the design rationale, dynamic light scattering (DLS) measurements gave an average hydrodynamic diameter of 18.4 $\pm$ 6.6 nm for TecVir at micro-molar concentrations (200 μM, Figure s1A), suggesting the formation of assemblies below 15 nm in size. Given that DLS is limited in size resolution to the factor of 3 and may not resolve complex and narrow size distributions, we sought more precise structural measurements. For the same concentrations, cryogenic transmission electron microscopy (cryo-TEM) revealed

abundant and monodisperse (12 ± 1.5 nm) spherical shells (Figure 2). The sizes appeared to hold at concentrations above the critical aggregation concentration (CAC) of TecVir (Figure s1B), below which ($\sim$75 μM) no apparent changes in light scattering intensity were observed (Figure s1C). This tendency correlated with low intercepts in DLS correlograms (Figure s1D), which were deemed unsuitable for the analysis of the assembly, suggesting it being incomplete at concentrations below CAC.[11] Intriguingly, the found CAC values and shell sizes proved to correlate within the ranges reported for charged spheroids assembled from orthogonally aligned helical copolypeptides, suggesting that TecVir shells should have a spherical morphology.[33]

To probe the morphology of the TecVir shells, cryo-electron tomographic reconstructions[34] of the obtained images were performed and returned spherical shells for TecVir (Figure 3A,B). With cryo-EM reconstructions providing attainable resolution in the 5−10 nm range,[35] which borders the size of TecVir shells, we performed 3D volume reconstructions of the images with the Chimera molecular graphics package[36] and benchmarked these against larger (>100 nm) shells of HIV-1 core assembly[37] that was used for comparison (Figure 3C).

The obtained reconstructions support the assembly of spherical, hollow shells. To provide complementary evidence of a similar resolution, but directly in solution, small-angle X-ray scattering (SAXS) was carried out. SAXS data were fitted for polydisperse structures including homogeneous cylinders. The fitting revealed a dominating external radius of a spherical shell (R_1) centered at 6.5 ± 2.3 nm and a wall thickness (th_1) of 4 nm together with an additional R_2 of 11.6 ± 5 nm with a th_2 of 5.8 nm (Figure 4A,B, Table s2).[38] The values for the two spherical shells overlapped and were in good agreement with the cryo electron microscopy and tomography data confirming that the vesicles were largely monodisperse and hollow.[11,39] The wall thickness of the shells matches the span of the coiled-coil building blocks of the design (4−4.4 nm), which is indicative of peptides orientating parallel to the axis of rotation in the shells as shown in Figure 1C,D. The fitting of the SAXS profile also incorporates a contribution from rod-like 4×2 nm cylinders. This finding agrees with the dimensions of the individual coiled-coil subunits (4×2 nm)[28,29] that remained in equilibrium with the assembled shells (Table s2), and is characteristic of cooperative and reversible assemblies.[40,41]

Circular dichroism (CD) spectroscopy confirmed appreciable helix formation for the assembly while spectral $\Delta\varepsilon_{222}/\Delta\varepsilon_{208}$ ratios were ≥1, as expected for helical oligomers as opposed to monomeric helices (Figures 4C, s2A).[42] The assembly proved to be highly cooperative as judged by sigmoidal unfolding curves with a single transition midpoint (T_M) of $\sim$55 °C (Figure s2B). Such a stable structure was found to be fully reversible with spectra recorded before and after the melt being nearly identical. During thermal denaturation (20−90 °C), the signal intensity at 202 nm remained the same providing a clear isodichroic point indicating a two-state transition between helical and unfolded forms (Figure s2A). In contrast, an Arg → Ala mutant of the peptide, TecVir[ala], designed as a negative control incapable of self-assembly did not fold or assemble (Figure 4C and Table s1). TecVir with the cysteine residue capped via thioalkylation, TecVir[cap], did fold, as expected, but the first derivatives of its unfolding curves suggested overlapping conformer populations with a predominant T_M of 65 °C (Figure s2C).

In accord with the data, atomic force microscopy, which provides an ideal probe for the analysis of morphologically
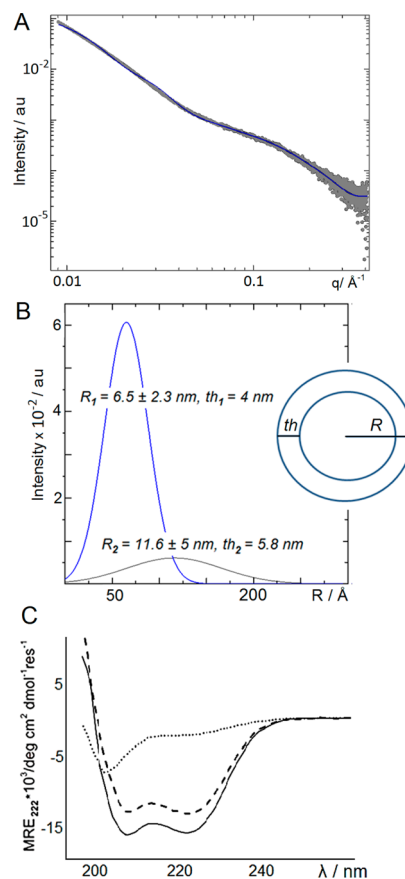
Figure 4. TecVir folding. (A) SAXS profile (gray dots) for TecVir shells (200 μM) and (B) Gaussian distributions corresponding to the radii (R) and wall thicknesses (th) of two hollow spheres (blue and gray). The fitting curve (dark blue) in (A) incorporates contributions from the two spheres and a 4×2 nm cylinder (coiled-coil dimer). (C) CD spectra for TecVir (—), TecVir[cap] (− − −), and TecVir[ala] (···): 100 μM peptide incubated overnight in 10 mM MOPS (pH 7.4) at 20 °C.

heterogeneous assemblies, revealed coexistent morphological forms: polydisperse particles and more anisotropic assemblies, extended nanofibers (Figure s3). The higher T_M of TecVir[cap] when compared to that of TecVir may therefore be attributed to the higher persistence length of the nanofibers, which were thicker and longer than TecVir shells, and whose assembly is likely enabled by helices lining up into longer, albeit noncovalent, superhelical strands.[32,43] This finding is in agreement with the stabilization effect of the cysteine residues on the assembly of the coiled-coil networks and with the formation of disulfide bridges. Indeed, the comparative quantification of free thiols in TecVir by Ellman's test gave up to 100% reductions in the concentration of free thiols in the assembly, confirming that cysteine residues were oxidized. The combined results indicate that TecVir folds into a hierarchical network supporting the formation of homogeneous nanoscale shells. The results obtained also permit approximate estimations regarding the number of coiled-coil dimers per shell. With the obtained radius of 6.5 nm (Figure 4B) and coiled-coil dimers (2×4 nm) arranged into tecto-dendrimer units (Figure 1C), a TecVir shell would assemble from $\sim$180 helices or 90 coiled-coil dimers (see Materials and Methods). The number of coiled-coil subunits involved in the assembly upon reaching its CAC can be expressed as an aggregation number, which in viruses reflects the number of protein subunits.[44,45] In viruses, however, it is nucleic acids and their encapsulation into viral
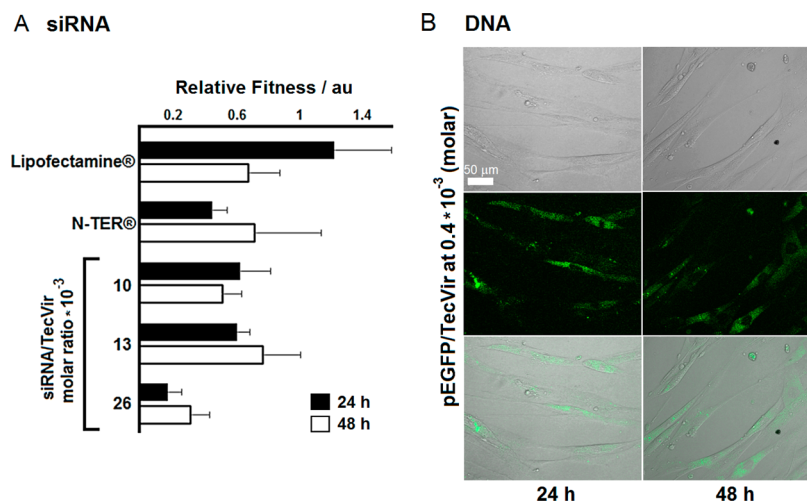
Figure 5. TecVir biological activity. TecVir-promoted gene transfer, expression (DNA), and silencing (siRNA). (A) Knockdown fitness of TecVir and commercial Lipofectamine RNAiMAX and N-TER (positive controls) normalized against siRNA alone (negative control) and the total counts of viable cells at different siRNA/TecVir molar ratios at 37 nM siRNA. (B) Widefield (upper), fluorescence (middle), and combined (lower) micrographs of human dermal fibroblasts transfected with plasmid DNA encoding for green fluorescent protein (green). GFP expression measured after 24 and 48 h is shown.

shells that determine biological function. Therefore, to be functional, viral mimetics must encase nucleic acids and infect cells.

Functional RNA and DNA Transfection. To gain an insight into its biological relevance, TecVir was probed for gene delivery. With the net charge of −3 (Table s1), TecVir assembles into anionic shells (ζ-potential of −42.4 ± 0.73 mV), which, unlike for most gene-delivery agents, disfavors purely electrostatic complexation with negatively charged nucleic acids. Therefore, encapsulation is necessary. TecVir does not incorporate specific motifs that can recognize and bind to nucleic acids. The free N-terminus of the peptide carries a free positive charge. Therefore, each coiled-coil unit contributes a double positive charge, allowing shell units to assemble around DNA or RNA, although at the expense of low nucleic-acid/peptide (N/P) ratios.

Indeed, TecVir that coassembled with small interfering RNA (siRNA) at N/P molar ratios of 1/40−1/100 promoted appreciable inhibition of targeted gene expression (Figure 5A). At these ratios, the size of TecVir assemblies increased to a mean diameter of 26.5 ± 8.7 nm (Figure 3A,B and Figure s4), with the shells remaining anionic (ζ-potential of −34.9 ± 0.9 mV). Given that the siRNA duplexes used in the study are ∼7.5 nm in length (23 bases) and 2 nm (B form) in diameter,[46] the interior diameter of an individual TecVir shell (4 nm) has to double in size to accommodate one or two siRNA duplexes, which appeared to be consistent with the overall size increases (Figure 1D).

These siRNA-containing assemblies promoted an active siRNA delivery showing cytoplasmic spreads of fluorescent siRNA that remained stable within the first hours of transfection, suggesting an endocytic uptake (Figure s5A). The siRNA/TecVir assemblies mediated gene knockdown, which was monitored by reverse transcription polymerase chain reaction (RT-PCR) at the mRNA level using HeLa cells with two housekeeping genes, ACTB (β-actin, targeted) and GAPDH (reference).[47] The silencing of β-actin mRNA was detected at 24 ± 2 and 48 ± 2 h post-transfection, with knockdown efficiency being comparable to that of commercial peptide (N-Ter) and liposomal (Lipofectamine RNAiMAX) reagents (Figure 5A). Higher N/P ratios gave negligible knockdown levels, while no obvious increases were observed for lower N/P ratios. By marked

contrast, siRNA/TecVir complexes that were attempted by adding siRNA into preassembled TecVir shells failed to yield reproducible knockdown, confirming that coassembly and encapsulation are necessary for siRNA delivery.

Monodispersity for viruses is a constraint ensuring the encapsulation of viral genes. Viral capsids tend to resist increases in cargo sizes, but may adapt by increasing the outer diameters through capsid packing adjustments.[48] The opposite is also true. Different cargoes, including nongenomic entities, can constrain a virus assembly into smaller particles while maintaining monodispersity.[27] In such cases, viruses adapt by tuning their packing symmetry to compensate for changes in size and hence the number of capsid proteins. For instance, a stimuli-responsive protein cargo can convert Cowpea Chlorotic Mottle Virus (CCMV) from 28 nm T = 3 capsids consisting of 180 proteins into 18 nm T = 1 shells assembled from 60 proteins.[49] This and other examples indicate that viruses can accommodate cargoes without compromising on homogeneity.[26] Similarly, the TecVir shells loaded with siRNA increased in sizes by at least doubling the number of dimeric coiled-coil subunits from 90 to 180 (see Materials and Methods). Interestingly, this effect appears to mirror the above example of CCMV, while being consistent with other RNA viruses of comparable sizes (e.g., the bacteriophage MS2 assembled from 180 protein subunits). This indicates that TecVir assemblies, although remaining uniform and homogeneous in size, are also structurally adaptable for encapsulating a larger genetic cargo. To test this, TecVir was coassembled with a large plasmid DNA encoding for the enhanced green fluorescent protein (pEGFP) to transfect primary cells, human dermal fibroblasts (Figure 5B). Strikingly, lower N/P molar ratios, as expected for larger nucleic acids, gave transfection efficiencies comparable to those of a liposomal reagent Lipofectamine 2000, while EGFP expression peaked at 80% of the total cells, within 48 h of incubation for both reagents with no apparent changes in cell morphology (Figures 5B and s5B). Biological activity (EGFP expression and mRNA silencing) was not associated with cytotoxic effects. In addition to unaltered cell morphology during transfections (Figure 5B), cell viability AlamarBlue assays, which provide quantitative indicators of metabolically active cells, confirmed that TecVir-treated cells remained viable over the entire

transfection periods (up to 48 h) (Figure s5C). This was in contrast to the control reagents (Lipofectamine 2000 and N-Ter), for which impaired cell viability was apparent (Figure s5C).

Taken together, the results from the biological tests show that TecVir shells effectively transfect cells and promote gene silencing and expression without imposing cytotoxic effects. The shells are highly anionic and lack known cell-adhesion motifs. Therefore, their uptake into the cells is likely to be analogous to that of similarly sized anionic polymeric dendrimers that tend to undergo a nonreceptor, caveolae-mediated endocytosis.[50] It is also consistent with that TecVir shells exhibit preference for an endocytic uptake (Figure s5) and may become endocytosed before entering the cytoplasm. To gain a better insight into this scenario, cells were preincubated with 50 mM NH₄Cl to block endosomal acidification and thence the cytoplasmic delivery of the shells.[51] Following this and subsequent transfection with AF647-siRNA/TecVir, fluorescence microscopy revealed notable increases in AF647 fluorescence for the pretreated cells when compared to that of NH₄Cl-free cells (Figure s6). These increases correlated with increased punctate fluorescence in the pretreated cells, indicating that the siRNA-loaded shells were indeed entrapped in the alkalinized endosomes (Figure s6B). The results are in accord with that TecVir shells in acidic endosomes, that is, under native transfection conditions, are fully protonated and positively charged (Table s1). More specifically, with pK_a ranges for the side chains of glutamates (4−5), cysteines (8−9), arginines (12−13), and for N-terminal amines (9−10), the proton affinities of arginines stay high at virtually any pH.[52] By contrast, glutamates become protonated only at acidic pH, which should compromise intra-helical ($g−c$) and inter-helical ($c−e'$) interactions (Figure 1). At neutral and alkaline pH, these interactions remain unchanged, as should the α-helical content of the TecVir assembly. Indeed, this proved to be the case. CD spectra of the assembly showed gradual decreases in helicity with decreasing pH, whereas no apparent changes were observed for higher pH values (Figure s7A). This trend also agrees with cystines reducing to cysteines at acidic pH, thus destabilizing the assembly further. As shown by TecVir^cap, disulfide bonds are important for the assembly of homogeneous and monodisperse TecVir shells. At acidic pH, TecVir unfolds, whereas most cystines become reduced. Inevitably these changes should lead to reduced shell numbers and disassembly. Gratifyingly, as gauged by cryo-TEM, no appreciable shell formation or other assemblies were observed for TecVir at acidic pH (Figure s7B).

The pH-responsive behavior of TecVir prompts a conclusion that in the acidic environments of endosomes, TecVir disassembles down to peptide monomers that then may act in a mode similar to that of amphipathic helical domains of nonenveloped viruses that disrupt endosomal membranes and induce egress of the cargo into the cytoplasm.[53]

CONCLUSION

In summary, by combining the principles of chemical and de novo design, we have engineered self-assembling peptide shells as structural and functional mimetics of viruses. These are compact and small structures that can adapt to encapsulate and transfer genetic material into human cells. Similar to viruses, these shells self-assemble from individual subunits and promote functional gene transfer into live cells without cytotoxicity effects common for commercial nonviral systems.[54]

Unlike viral subunits, which are large and conserved proteins, TecVir is built of much smaller peptides. This is beneficial for the development of bespoke artificial viruses because peptides are

more synthetically accessible, their chemistry allows substantial orthogonality for topology and functionalization, while peptide folding-assembly pathways can be predictably engineered using basic protein folding motifs.[55] In assembly terms, the TecVir topology may further be optimized by, for example, reducing its CAC, which for peptidic viral mimetics can be effectively tailored to nanomolar ranges.[11,25] In functional terms, TecVir forms virus-like nanoshells with pI (4.5) that falls within the range of viral isoelectric points of 3.5−7.[56] This property holds a particular promise for engineering small anionic virions with the ability to cross blood brain barrier or circumvent rapid clearance from circulation and cytotoxicity, which for cationic reagents remain major obstacles toward effective gene therapy approaches.[57]

■ MATERIALS AND METHODS

Peptide Synthesis and Purification. All peptides were assembled on a Liberty microwave peptide synthesizer (CEM) using standard Fmoc/^tBu solid-phase protocols with HBTU/DIPEA as coupling reagents on a Rink amide resin. Following postsynthesis cleavage and deprotection (95% TFA, 2.5% TIS, 2.5% EDT), the peptides were purified by semipreparative reversed-phase high-performance liquid chromatography (RP-HPLC).

For S-alkylation, TecVir was denatured in 8 M urea, 0.6 M Tris-HCl, and 5 mM EDTA (pH 8.6) flushed with N₂ gas. The peptide was reduced using a 100-fold molar excess of β-mercaptoethanol for 2 h at 40 °C in a N₂ atmosphere. Alkylation using freshly prepared iodo-acetamide at 130-fold molar excess was performed for 15 min in the dark. The peptide was purified using dialysis against water overnight in the dark with MALDI-MS used to confirm alkylation.

The identities of the peptides were confirmed by analytical RP-HPLC and MALDI-ToF mass spectrometry. MS [M + H]⁺: TecVir, m/z 3500.9 (calc), 3500.3 (found); TecVir^ala, m/z 3160.5 (calc), 3160.7 (found); TecVir^cap, m/z 3557.9 (calc), 3558.9 (found).

Analytical and semipreparative RP-HPLC was performed on a JASCO HPLC system (PU-980; Tokyo, Japan), using a Vydac C18 analytical and semipreparative (both 5 μm) columns. Both analytical and semipreparative runs used a 10−60% B gradient over 30 min at 1 and 4.5 mL/min, respectively, with detection at 280 and 214 nm (buffer A, 5% and buffer B, 95% aqueous CH₃CN, 0.1% TFA). The samples for analytical runs were preincubated for 60 min in the buffer A containing TCEP (50 mM).

Circular Dichroism (CD) Spectroscopy. Aqueous peptide solutions at 100 μM (300 μL) were prepared in filtered (0.22 μm) 10 mM MOPS, pH 7.4, at 20 °C, overnight. Stock solutions were in water or 1 mM TCEP. CD experiments were performed on a JASCO J-810 spectropolarimeter fitted with a Peltier temperature controller. All measurements were taken in ellipticities in mdeg and after baseline correction were converted to mean residue ellipticity by normalizing for the concentration of peptide bonds and cuvette path length. The data collected with a 1 nm step and 1 s collection time per step are presented as the average of 4 scans. Thermal denaturation curves were recorded at 2 °C intervals using 1 nm bandwidth, with the signal averaged for 16 s and with a 2 °C/min ramp rate. pH dependence experiments were performed in 10 mM sulfonate buffers (EPPS, basic; MOPS, neutral; MES acidic) and by direct titrations to peptide samples in MOPS, giving similar results.

Small-Angle X-ray Scattering (SAXS). Experiments were performed at the synchrotron SAXS beamline B21 (Diamond Light Source, UK). A few microliters of samples was injected via an automated sample exchanger at a slow and very reproducible flux into a quartz capillary (1.8 mm internal diameter), which was then placed in front of the X-ray beam. The quartz capillary was enclosed in a vacuum chamber, to avoid parasitic scattering. After the sample was injected in the capillary and reached the X-ray beam, the flow was stopped during the SAXS data acquisition. B21 operated with a fixed camera length (4 m) and fixed energy (12.4 keV) allowing data collection for $q = 0.009−0.4$ Å⁻¹ ($q = 4\pi$ sin Θ/λ, with Θ as the scattering angle and $\lambda = 1$ Å). The images were

captured using a Pilaturs 2 M detector. Data processing (background subtraction, radial averaging) was performed using dedicated beamline software Scatter.

The SAXS intensity was modeled using Sasfit software,[38] considering the contribution of spherical shells with two different size distributions coexisting with cylinders in solution. Briefly, the spherical shell model considers the overall radius of the spherical shell, R_o, the core radius, $R_i = \nu \cdot R_o$ (where ν is a fraction of the overall radius), and the scattering length density difference between the shell and matrix, $\Delta\eta$.[38] The model considers the contribution of two populations of spherical shells with Gaussian distributions for R_o, with each Gaussian distribution having a standard deviation, σ. The model considers homogeneous, solid cylinders, with a radius R_c, a length L, and a scattering contrast $\Delta\eta_c$. Fitting parameters and values, including the wall thickness $th = R_o - R_i$, are summarized in Table s2. A constant background value (3×10^5) was used in the model.

Cryogenic Transmission Electron Microscopy (Cryo-TEM). Cryo-TEM samples were prepared by plunge-freezing using a VITROBOT mark IV (FEI Co.) in liquid ethane cooled with liquid N₂. Solution droplets (5 μL) of TecVir (100−200 μM) or siRNA/TecVir at stated ratios at 200 μM peptide, prepared in MOPS (10 mM, pH 7.4, overnight), were placed on glow discharged Lacey carbon grids and left for 2 s before blotting (2 s) and plunging. This gave samples with TecVir particles embedded in the vitreous ice suspended inside the holes of the carbon. The sample grid was then transferred (without warming) into a Gatan 626 cryo-holder and observed at 200 kV in a Tecnai T20 (FEI Co.) transmission electron microscope fitted with an Eagle 4 k × 4 k camera (FEI). Cryo-TEM images were analyzed using Fiji analysis software. TecVir dimensions were characterized by applying a bandpass filter, thresholding, and the "analyze particle" function, using Fiji image analysis software. The data derived from the analysis were confirmed by comparing with dimensions obtained directly from the raw images. Size distributions were measured for over 10^3 shells.

Cryo-TEM Tomography. Samples were prepared as above, and tilt series were collected automatically at 3° increments over an angular range of −55° to 55° for siRNA/TecVir and −42° to 55° for TecVir. The electron dose was 1.7 and 2.75 electrons/Å²/s/image, respectively, for siRNA/TecVir and TecVir, at an average 1 s exposure, giving a total dose of 63 and 91 electrons/Å², respectively, that is, true low dose conditions. Tomograms were reconstructed from the tilt series with IMOD,[34] using carbon grid tracking for alignment. The isosurface and volume views were rendered after Gaussian low-pass filtering and removal of isolated noise densities in CHIMERA (http://www.cgl.ucsf.edu/chimera/).

Atomic Force Microscopy. For AFM imaging, a drop (5 μL) of peptide solution prepared as above was placed on a clean silicon wafer, and the buffer excess was removed by blotting paper. All measurements were carried out using tapping mode AFM on a Cypher instrument (Asylum research) using supersharp silicon probes (SSS-NCHR, Nanosensors; resonant frequency ∼330 kHz, tip radius of curvature <5 nm, force constant 42 N/m). Images were flattened via line-by-line subtraction of first-order fits to the background, using SPIP software, version 6.0.2.

Photon Correlation Spectroscopy. Zetasizer Nano (ZEN3600, Malvern Instruments Ltd., Worcestershire, UK) was used to measure size distributions, scattering intensity, and ζ-potential in folded capillary cells at 25 °C. Hydrodynamic radii and ζ-potential values were obtained through the fitting of autocorrelation data using the manufacture's software, Zetasizer Software (version 7.03). The ζ-potential values reported for the assembled TecVir are a mean of two independent preparations each measured in triplicate, with each measurement consisting of 10 recordings. Size distributions and CAC values represent a mean of three independent preparations each measured in quintuplicate with a 2 min delay for each measurements, with each measurement consisting of 20 recordings.

Determination of Free Thiols. A stock solution of 5,5′-dithiobis(2-nitrobenzoic acid) (Ellman's reagent from Pierce) was prepared to a final concentration of 2 mM in LC-MS grade water with 50 mM sodium acetate. 50 μL of the solution was mixed with 10 mM MOPS (pH 7.4, 100 μL) and LC−MS grade water (840 μL), to take

background absorbance. TecVir (10 μL, 100 μM) was then added to the solution (final volume of 1 mL). 200 μL of the final solution was scanned in the 280−600 nm region (automatic background subtraction) with recording absorbance at 412 nm. Absorbance for each sample was calculated, and the results were averaged and divided by 14 150/M cm (extinction coefficient of 2-nitro-5-thiobenzoate) and 1 (number of thiols in peptide) to obtain final concentrations. Free thiol was quantified using a cysteine standard curve prepared according to the proprietary protocol.

Estimations for the Number of Coiled-Coil Subunits per Shell. Given that a coiled-coil dimer spans 2 nm in diameter, the surface area of a hexagonal branching cell in Figure 1C is 10.4 nm². A tecto-dendrimer unit consists of seven asymmetric hexagons (Figure 1C), which gives a surface area of ∼73 nm². Dividing this value by the number of helices in the unit (24) gives the area taken by a single helix monomer (∼3 nm²). The surface area of a shell with the found radius of 6.5 nm would be ∼531 nm², which when divided by the area of a helix gives the total of 180 helices in a shell, or 90 coiled-coil dimers. Similarly, siRNA-loaded TecVir shells are 26.5 nm in diameter. Given that the wall thickness of a shell is 4 nm (Figure 4B), the inner lumen of a siRNA-loaded shell has a diameter of 18.5 nm, with the inner surface area being 1075 nm². To cover this area would require ∼180 coiled-coil dimers, which is at least double what is required for the empty shells.

Transfection and Knockdown Assays. HeLa cells were maintained in DMEM cell culture medium supplemented with serum growth supplement and antibiotics (gentamicin and amphotericin B) in 25 cm² culture flasks, and grown at 37 °C, 5% CO₂ for 24 h to reach 60% confluency. The cells were then washed (×3) with PBS and trypsinized followed by the addition of trypsin inhibitors to eliminate secondary toxic effects of trypsin. Detached cells were spun down by centrifugation, and the excess solvent was replaced by cell growth media. Ten microliters of cell solution was mixed with 10 μL of Trypan blue. The mixture was then placed on a counting plate to count cells (25×10^3 cells per well). Before transfection, the cells were washed (×3) with OptiMEM-Serum reduced media.

mRNA Concentrations. In cells transfected with siRNA/TecVir and controls these were measured according to the MIQE guidelines.[47] Lipofectamine and N-TER were used as positive controls and prepared according to the proprietary protocols. The knockdown assay was performed using two recommended housekeeping genes, ACTB (targeted) and GAPDH (reference). siRNA alone was used as a negative (background) control. Proprietary primers (design optimized for PCR), RNA extraction, and RT-qPCR kits together with method development protocols were adapted to limit assay optimization. All measurements were done in triplicate.

siRNA Transfections for Knockdown. β-Actin siRNA (30 pmole) was used for transfection with peptide concentration adjusted to the desired N/P. Preparations with siRNA added into peptide after or before the assembly were similar. siRNA was incubated with peptide in MOPS (20 μL, 10 mM, pH 7.4, overnight) followed by incubations in OptiMEM (200 μL). Prepared siRNA/TecVir or controls were added to cells and incubated for 3 h. After these 3-h incubations, the cells were supplemented with complete DMEM media (20% serum, 200 μL). Further incubations were performed over 48 h marking different time points. For RNA extraction, cells were harvested as described above, RNA was prepared using mini RNeasy mini prep kit, and cDNA was prepared from the RNA using the QuantiTect reverse transcription kit and quantified using two-step RT-qPCR dual hybridization with a QuantiFast probe assay kit (all from Qiagen, U.S.). The PCR hydrolysis probes for β-actin and GAPDH labeled with FAM and MAX dyes were used as per the proprietary protocols (Qiagen).

pDNA Transfections. These were performed as above on human dermal fibroblasts using plasmid DNA encoding for eGFP (500 ng). Lipofectamine 2000 was used as a positive control. After transfections were complete (24, 48 h), the wells were visualized using confocal microscopy. Transfection efficiencies were assessed and expressed as the total fluorescent cell counts (GFP) of the total cell counts (100%) (Figure s5).

siRNA Transfection over First Hours. Alexa 647-labeled siRNA (Eurogentec, UK) was used to visualize transfections during first

hours. siRNA/TecVir and siRNA/Lipofectamine were incubated with HeLa cells for 3 h, after which the medium was replaced with serum supplemented complete medium to allow further 3-h incubations. Fluorescence was then measured using an Olympus FW-100 confocal microscope, and obtained micrographs were analyzed using ImageJ software. After the background fluorescence was subtracted, transfection efficiencies were expressed in percentage as a total count of fluorescent cells, with the total cell count taken as 100% (Figure s5).

RT-qPCR. Cells harvested from a single well were lysed (10^5 cells in 350 μL of lysis buffer), and total RNA was purified (RNeasy mini). RT was performed (QuantiTect) in PCR 0.2 mL tubes on a GeneAmp PCR system 2700 (Applied Biosystems, UK) using 30−60 ng of total RNA according to the proprietary protocols. qPCR was performed on a SmartCycler using Software v2.0d (Cepheid). PCR of the diluted cDNA product (1−10 ng) was monitored over 45 cycles with the quantification cycle (C_q) determined using a manual threshold of 30 fluorescence units. PCR titrations of both genes resulted in colinear amplification. Control samples of no template control (contamination during qPCR) and no RT control (contamination by genomic DNA during RT) were negative ($C_q > 35$ cycles), indicating no measurable DNA contamination. Fitness levels were calculated on the basis of the normalized function of cells treated with siRNA alone (negative control) and against the total counts of viable cells (cell viability):

$$= \frac{\Delta\Delta C_T}{(\text{cell count/cell count for siRNA only control})}$$

where $\Delta\Delta C_T$ is the knockdown efficiency of ACTB (i) relative to reference GAPDH gene for each transfection vector ($\Delta C_T(\text{vector})$):

$$\Delta C_T(\text{vector}) = C_T(\text{ACTB}) - C_T(\text{GAPDH})$$

where the threshold cycle (C_T) is calculated from the PCR thermal cycle; and (ii) relative to the siRNA only control ($\Delta C_T(\text{siRNA only control})$):

$$\Delta\Delta C_T = \Delta C_T(\text{vector}) - \Delta C_T(\text{siRNA only control})$$

Poisoned Transfection. This growth medium was removed from wells containing HeLa cells after overnight incubation allowing for cell attachment. 200 μL of Opti-MEM preincubated at 37 °C and containing either just Opti-MEM (controls) or 50 mM NH_4Cl was added to cells. These samples were further incubated for 30 min at 37 °C under 5% CO_2. After the preincubation, AF647-siRNA/TecVir (13×10^{-3} molar ratio) was added to each well and incubated for 3 h at 37 °C under 5% CO_2. Confocal fluorescence microscopy (633 nm laser) was used to visualize AF647-siRNA. Recorded images were processed using Fuji ImageJ software.

Confocal Fluorescence Microscopy. Images were acquired using a confocal laser scanning microscope (CLSM) (FV-1000, Olympus). Live cell imaging was performed under controlled environmental conditions (37 °C, 5% CO_2). Images (2D and 3D stacks) were processed using Imaris v5.1 and ImageJ software.

Cell Viability Assay. HeLa cells were seeded in a 96-well plate at 4000 cells per well and incubated overnight at 37 °C, 5% CO_2. After incubation, control transfection reagents (loaded with siRNA according to the proprietary protocols) or TecVir assembled in 10 mM MOPS (pH 7.4) at different concentrations were added (10 μL), and diluted with Opti-MEM to a final volume of 100 μL. After 3-h incubations, 100 μL of DMEM cell culture medium was added to each well, and the plates were incubated for 24 and 48 h. AlamarBlue reagent (ThermoFisher Scientific) was supplied as a 10× solution and added to each well by diluting (1×) in the culture medium. The cells were incubated for 2 h at 37 °C in 100 μL of the reagent. The fluorescence of each well was measured with a microplate reader (BMG Labtech, Germany), with 544 nm excitation and 590 nm emission filters. Standard calibration curves (200−20 000 cells) were generated by plotting measured fluorescence values versus cell numbers. Total viable cell counts are expressed in percentage after subtracting the total cell counts measured for samples without transfection reagents (control). All measurements were done in triplicate.

Statistical Analysis. This was performed by OriginPro 8.5 using ANOVA followed by a Fisher post-test for three independent experiments each done in triplicate, with p values <0.05 considered significant. The results are expressed as an average ± standard deviation.

■ ASSOCIATED CONTENT

Ⓢ Supporting Information

The Supporting Information is available free of charge on the ACS Publications website at DOI: 10.1021/jacs.6b05751.

Tables and figures as described in the text (PDF)

■ AUTHOR INFORMATION

Corresponding Author
*max.ryadnov@npl.co.uk

Notes
The authors declare no competing financial interest.

■ ACKNOWLEDGMENTS

■ REFERENCES

(1) Perlmutter, J. D.; Hagan, M. F. *Annu. Rev. Phys. Chem.* **2015**, *66*, 217.

(2) Yin, S.; Sun, S.; Yang, S.; Shang, Y.; Cai, X.; Liu, X. *Virol. J.* **2010**, *7*, 166.

(3) Philippe, N.; Legendre, M.; Doutre, G.; Couté, Y.; Poirot, O.; Lescot, M.; Arslan, D.; Seltzer, V.; Bertaux, L.; Bruley, C.; Garin, J.; Claverie, J. M.; Abergel, C. *Science* **2013**, *341*, 281.

(4) Mastrobattista, E.; van der Aa, M. A.; Hennink, W. E.; Crommelin, D. J. *Nat. Rev. Drug Discovery* **2006**, *5*, 115.

(5) Marsden, H. R.; Korobko, A. V.; van Leeuwen, E. N. M.; Pouget, E. M.; Veen, S. J.; Sommerdijk, N. A. J. M.; Kros, A. *J. Am. Chem. Soc.* **2008**, *130*, 9386.

(6) Ni, R.; Chau, Y. *J. Am. Chem. Soc.* **2014**, *136*, 17902.

(7) Olson, A. J.; Hu, Y. H. E.; Keinan, E. *Proc. Natl. Acad. Sci. U. S. A.* **2007**, *104*, 20731.

(8) Nakai, T.; Kanamori, T.; Sando, S.; Aoyama, Y. *J. Am. Chem. Soc.* **2003**, *125*, 8465.

(9) Holowka, E. P.; Sun, V. Z.; Kamei, D. T.; Deming, T. J. *Nat. Mater.* **2007**, *6*, 52.

(10) Lamarre, B.; Ryadnov, M. G. *Macromol. Biosci.* **2011**, *11*, 503.

(11) Matsuura, K.; Watanabe, K.; Matsuzaki, T.; Sakuri, K.; Kimizuka, N. *Angew. Chem., Int. Ed.* **2010**, *49*, 9662.

(12) Tarasov, S. G.; Gaponenko, V.; Howard, O. M.; Chen, Y.; Oppenheim, J. J.; Dyba, M. A.; Subramaniam, S.; Lee, Y.; Michejda, C.; Tarasova, N. I. *Proc. Natl. Acad. Sci. U. S. A.* **2011**, *108*, 9798.

(13) Matsuura, K.; Murasato, K.; Kimizuka, N. *J. Am. Chem. Soc.* **2005**, *127*, 10148.

(14) Castelletto, V.; De Santis, E.; Alkassem, H.; Lamarre, B.; Noble, J. E.; Ray, S.; Bella, A.; Burns, J. R.; Hoogenboom, B. W.; Ryadnov, M. G. *Chem. Sci.* **2016**, *7*, 1707.

(15) King, N. P.; Bale, J. B.; Sheffler, W.; McNamara, D. E.; Gonen, S.; Gonen, T.; Yeates, T. O.; Baker, D. *Nature* **2014**, *510*, 103.

(16) Frechet, J. M. J. *Proc. Natl. Acad. Sci. U. S. A.* **2002**, *99*, 4782.

(17) Caminade, A.-M.; Yan, D.; Smith, D. K. *Chem. Soc. Rev.* **2015**, *44*, 3870.

(18) Lin, B. F.; Marullo, R. S.; Robb, M. J.; Krogstad, D. V.; Antoni, P.; Hawker, C. J.; Campos, L. M.; Tirrell, M. V. *Nano Lett.* **2011**, *11*, 3946.

(19) Uppuluri, S.; Swanson, D. R.; Piehler, L. T.; Li, J.; Hagnauer, G. L.; Tomalia, D. A. *Adv. Mater.* **2000**, *12*, 796.

(20) Tomalia, D. A.; Brothers, H. M.; Piehler, L. T.; Durst, H. D.; Swanson, D. R. *Proc. Natl. Acad. Sci. U. S. A.* **2002**, *99*, 5081.

(21) Ryadnov, M. G. *Angew. Chem., Int. Ed.* **2007**, *46*, 969.

(22) Fletcher, J. M.; Harniman, R. L.; Barnes, F. R.; Boyle, A. L.; Collins, A.; Mantell, J.; Sharp, T. H.; Antognozzi, M.; Booth, P. J.; Linden, N.; Miles, M. J.; Sessions, R. B.; Verkade, P.; Woolfson, D. N. *Science* **2013**, *340*, 595.

(23) Matsuura, K. *Polym. J.* **2012**, *44*, 469.

(24) Matsuura, K.; Watanabe, K.; Matsushita, Y.; Kimizuka, N. *Polym. J.* **2013**, *45*, 529.

(25) Matsuura, K.; Nakamura, T.; Watanabe, K.; Noguchi, T.; Minamihata, K.; Kamiya, N.; Kimizuka, N. *Org. Biomol. Chem.* **2016**, *14*, 7869.

(26) Glasgow, J.; Tullman-Ercek, D. *Appl. Microbiol. Biotechnol.* **2014**, *98*, 5847.

(27) Maassen, S. J.; van der Ham, A. M.; Cornelissen, J. L. M. *ACS Macro Lett.* **2016**, *5*, 987.

(28) Apostolovic, B.; Danial, M.; Klok, H.-A. *Chem. Soc. Rev.* **2010**, *39*, 3541.

(29) Lupas, A. *Trends Biochem. Sci.* **1996**, *21*, 375.

(30) Koronakis, V.; Sharff, A.; Koronakis, E.; Luisi, B.; Hughes, C. *Nature* **2000**, *405*, 914.

(31) Döbereiner, H.-G.; Selchow, O.; Lipowsky, R. *Eur. Biophys. J.* **1999**, *28*, 174.

(32) Ryadnov, M. G.; Woolfson, D. N. *J. Am. Chem. Soc.* **2007**, *129*, 14074.

(33) Holowka, E. P.; Pochan, D. J.; Deming, T. J. *J. Am. Chem. Soc.* **2005**, *127*, 12423.

(34) Kremer, J. R.; Mastronarde, D. N.; McIntosh, J. R. *J. Struct. Biol.* **1996**, *116*, 71.

(35) Diebolder, C. A.; Koster, A. J.; Koning, R. I. *J. Microsc.* **2012**, *248*, 1.

(36) Pettersen, E. F.; Goddard, T. D.; Huang, C. C.; Couch, G. S.; Greenblatt, D. M.; Meng, E. C.; Ferrin, T. E. *J. Comput. Chem.* **2004**, *25*, 1605.

(37) Briggs, J. A.; Grünewald, K.; Glass, B.; Förster, F.; Kräusslich, H. G.; Fuller, S. D. *Structure* **2006**, *14*, 15.

(38) Breßler, I.; Kohlbrecher, J.; Thünemann, A. F. *J. Appl. Crystallogr.* **2015**, *48*, 1587.

(39) Hirai, M.; Iwase, H.; Hayakawa, T.; Koizumi, M.; Takahashi, H. *Biophys. J.* **2003**, *85*, 1600.

(40) Zlotnick, A. *J. Mol. Biol.* **1994**, *241*, 59.

(41) Hernandez-Garcia, A.; Kraft, D. J.; Janssen, A. F.; Bomans, P. H.; Sommerdijk, N. A.; Thies-Weesie, D. M.; Favretto, M. E.; Brock, R.; de Wolf, F. A.; Werten, M. W.; van der Schoot, P.; Stuart, M. C.; de Vries, R. *Nat. Nanotechnol.* **2014**, *9*, 698.

(42) Kelly, S. M.; Jess, T. J.; Price, N. C. *Biochim. Biophys. Acta, Proteins Proteomics* **2005**, *1751*, 119.

(43) Papapostolou, D.; Smith, A. M.; Atkins, E. D.; Oliver, S. J.; Ryadnov, M. G.; Serpell, L. C.; Woolfson, D. N. *Proc. Natl. Acad. Sci. U. S. A.* **2007**, *104*, 10853.

(44) Carrillo-Tripp, M.; Shepherd, C. M.; Borelli, I. A.; Venkataraman, S.; Lander, G.; Natarajan, P.; Johnson, J. E.; Brooks, C. L.; Reddy, V. S. *Nucleic Acids Res.* **2009**, *37*, D436.

(45) Wick, C. H. *Integrated Virus Detection*; CRC Press: Boca Raton, FL, 2014.

(46) Schroeder, A.; Levins, C. G.; Cortez, C.; Langer, R.; Anderson, D. G. *J. Intern. Med.* **2010**, *267*, 9.

(47) Bustin, S. A.; Benes, V.; Garson, J. A.; Hellemans, J.; Huggett, J.; Kubista, M.; Mueller, R.; Nolan, T.; Pfaffl, M. W.; Shipley, G. L.; Vandesompele, J.; Wittwer, C. T. *Clin. Chem.* **2009**, *55*, 611.

(48) He, L.; Porterfield, Z.; van der Schoot, P.; Zlotnick, A.; Dragnea, B. *ACS Nano* **2013**, *7*, 8447.

(49) van Eldijk, M. B.; Wang, J. C. Y.; Minten, I. J.; Li, C.; Zlotnick, A.; Nolte, R. J. M.; Cornelissen, J. J. L. M.; van Hest, J. C. M. *J. Am. Chem. Soc.* **2012**, *134*, 18506.

(50) Perumal, O. P.; Inapagolla, R.; Kannan, S.; Kannan, R. M. *Biomaterials* **2008**, *29*, 3469.

(51) Potocky, T. B.; Menon, A. K.; Gellman, S. H. *J. Biol. Chem.* **2003**, *278*, 50188.

(52) Gronert, S.; Simpson, D. C.; Conner, K. M. *J. Am. Soc. Mass Spectrom.* **2009**, *20*, 2116.

(53) Wiethoff, C. M.; Wodrich, H.; Gerace, L.; Nemerow, G. R. *J. Virol.* **2005**, *79*, 1992.

(54) Breunig, M.; Lungwitz, U.; Liebl, R.; Goepferich, A. *Proc. Natl. Acad. Sci. U. S. A.* **2007**, *104*, 14454.

(55) De Santis, E.; Ryadnov, M. G. *Chem. Soc. Rev.* **2015**, *44*, 8288.

(56) Michen, B. T.; Graule, T. *J. Appl. Microbiol.* **2010**, *109*, 388.

(57) Tagalakis, A. D.; Lee, D. H.; Bienemann, A. S.; Zhou, H.; Munye, M. M.; Saraiva, L.; McCarthy, D.; Du, Z.; Vink, C. A.; Maeshima, R.; White, E. A.; Gustafsson, K.; Hart, S. L. *Biomaterials* **2014**, *35*, 8406.